Northern California Chapter of the Amercian Association of Physicists in Medicine

The Young Investigator's Symposium

Friday, May 1st, 2020

Via Zoom (Meeting ID: 906-148-533, Password: 2020YIS)

11:45 – 12:00 P.M. **Sign-In & Registration**

12:00 – 01:00 P.M. **Keynote Speech**

Dr. Lei Xing, Jacob Haimson Professor and The Director of Medical Physics Division, Stanford

"Artificial intelligence for medical physics and radiation oncology"

01:00 – 4:00 P.M. **Talks from young Investigators:**

Students:

Caylin Colson:

Evidence that SPIO Chain Formation is Essential for Super-Resolution MPI

K. L. Barry Fung:

Surface protein targeted molecular imaging approach for tracking white blood cells to inflammation using Magnetic Particle Imaging

Liyue Shen:

Novel-View X-ray Image Generation by Deep Learning through Multi-Domain Image Translation

Ignacio Romero

A feasibility study of Time of Flight Computed Tomography

Michael C Lun:

X-ray luminescence imaging for small animals

Postdocs:

Syamantak Khan

FLASH irradiation can spare in vitro multicellular spheroids by rapid radiolytic depletion of oxygen

Negar Omidavi

Lutetium Background Radiation in uEXPLORER Total-body PET Scanner: Applications and Challenges in Attenuation Correction

Young Investigator Program Director: Stan Benedict: shbenedict@ucdavis.edu
Young Investigator Program Co-Director: Amy Yu: amysyu@stanford.edu
Northern Calif Chapter AAPM: President: Jason Matney, Treasurer: Olga Stafford, Secretary: Lawrie Skinner, Board Member: Sarah McKenney

Residents:

Eric Simiele

Laser-like x-ray sources for a new SRS/SBRT paradigm

Levent Sensoy

A more accurate assessment of pulmonary 18F-FDG PET as an imaging biomarker for post-radiotherapy pulmonary toxicity through partial volume correction.

Matthieu Lafreniere

Continuous Generation of Volumetric Images During Radiation Therapy Using a 4DCT-Based Patient-Specfic Motion Model, Periodic kV Imaging and a Continuous External Respiratory Surrogate Signal

Tomi Nano

Reducing IMRT QA workload by 95% and keeping the same level of quality control

SLAM competitions:

Liyue Shen

Deep Learning-powered Few-view CT Image Reconstruction with Geometric Priors

Matthieu Lafreniere

Continuous Generation of Volumetric Images During Radiation Therapy Using a 4DCT-Based Patient-Specfic Motion Model, Periodic kV Imaging and a Continuous External Respiratory Surrogate Signal

Syamantak Khan

Customized cancer treatment using Tumor-Chips

Tomi Nano

Reducing IMRT QA workload by 95% and keeping the same level of quality control

04:30 – 5:00 P.M. **Award Ceremony**

Abstract Title:

Evidence that SPIO Chain Formation is Essential for Super-Resolution MPI

Authors:

Caylin Colson, Zhi Wei Tay, K.L. Barry Fung, Daniel W. Hensley, Shehaab Savliwala, Ben D. Fellows, Xinyi Y. Zhou, Yao Lu, Prashant Chandrasekharan, Carlos Rinaldi, Steven M. Conolly

Institution:

UC Berkeley – UCSF Graduate Program in Bioengineering

Abstract: (*Excluding accompanying data and images.*)
Recently published work can also be presented.

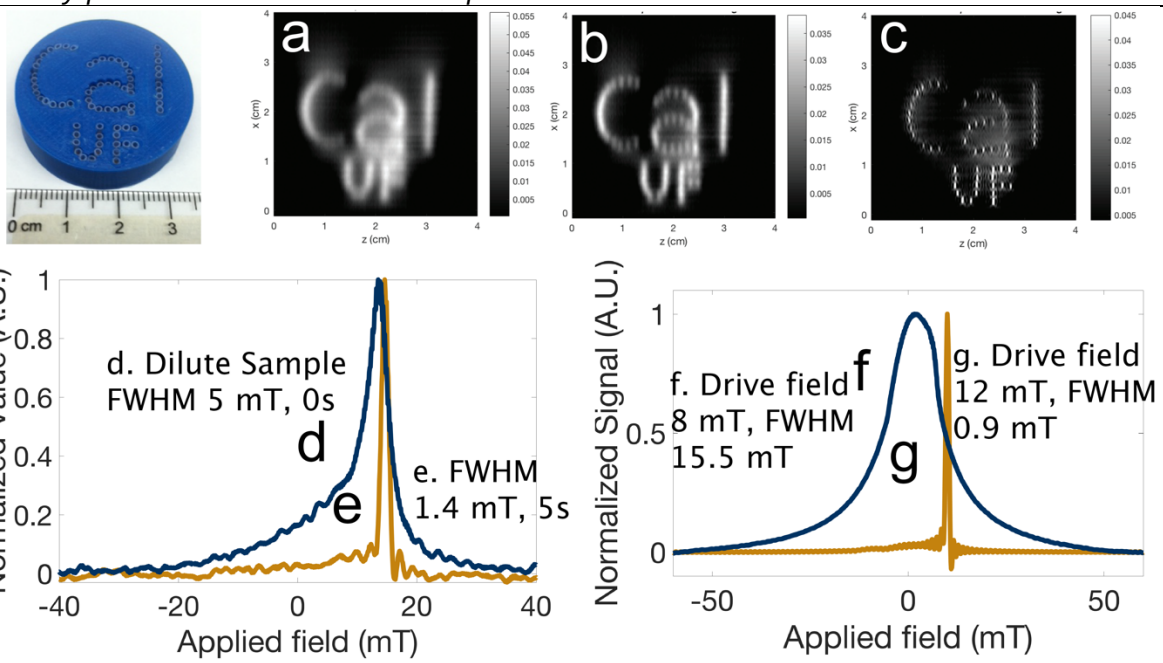

a) 1D Point Spread Functions showing experimental 6-fold improvement in spatial resolution (a to c) Conventional low-resolution MPI **b)** MPI scan with conventional single-core particles **c)** High Resolution siMPI scan **d)** Highly diluted sample does not show desired FWHM **e)** A pre-polarizing pulse applied before excitation gives 4-fold improvement in spatial resolution **f)** Traditional Langevin PSF is seen below "latching" amplitude **h)** Above the "latching" amplitude gives a 20-fold improvement in spatial resolution (a) 1.1 mg/mL Vivotrax, (b) (0.21 mg/mL LodeSpin-017) c)(25 ug/mL UF-UC Berkeley Emulsion) (d) 7.8 ug/mL, (f) 12.6 mg/mL.

Magnetic Particle Imaging (MPI) is a newly developed tracer-based modality with promising applications in molecular imaging, *in vivo* cell tracking, and clinical angiography. Because its unique physics takes advantage of the electronic magnetization of superparamagnetic iron oxide particles (SPIOs), MPI has an excellent safety profile, superb linear "positive contrast", ideal tissue penetration, and a sensitivity of 200 cells [1,2,3]. However, the spatial resolution of MPI is currently limited to roughly 1 mm in high gradient (up to 7 T/m) small animal scanners. To compete with preclinical MRI and CT, improving MPI resolution to roughly 100-microns would be an enabling

advance. Here we investigate a novel type of MPI tracer, which we call superferromagnetic particles (SFMIOs), which have experimentally yielded both a 10x improvement in resolution and a 100x improvement in SNR [4]. We test the hypothesis that "chaining" of strongly interacting SPIOs is essential for the dramatic improvement, and test this hypothesis by varying media viscosity, concentration, and pre-polarization fields to gauge their influence on SNR and spatial resolution.

See data in Fig. 1. At excitation amplitudes below ~12 mT, a traditional Langevin PSF is observed (FWHM ~ 18 mT). If the drive field amplitude exceeded the coercivity threshold (roughly 12 mT), the PSF became *dramatically* sharper (~1 mT FWHM). Similar nonlinear latching behavior was noted for viscosity, with far better resolution in lower viscosity medium. We observed a critical concentration threshold for the dramatic improvement in spatial resolution. Prepolarization pulses recovered the sharper PSF in below-concentration-threshold samples. We consistently observe ferromagnetic behavior from an assembly of SPIO nanoparticles. All of these observations support the chaining hypothesis for dramatic improvement in spatial resolution.

References:

[1] Gleich, Bernhard and Jurgen Weizenecker (2005). *Nature* 435, pp. 1214-1217.
[2] Goodwill, P. W., & Conolly, S.M. (2010). *IEEE Transactions on Medical Imaging*, 29(11), 1851-1859.
[3] Zheng, B., Vazin, T., Goodwill, P.W., Conway, A., Verma, A., Ulku Saritas, E.,..Conollu, S.M. (2015). *Scientific Reports,* 5.
[4] Tay, Zhi Wei. (2018). *Dissertation.*
[5] Vreeland, E. C., Watt, J., Schober, G.B., Hance, B. G., Austin, M.J., Price, A.D., ... Huber, D.L. (2015).*Chemistry of Materials*, 27(17), 6059-6066.
[6] Tay, Z. W., Goodwill, P.W., Hensley, D.W., Taylor, L.A., Zheng, B., & Conolly, S.M. (2016). *Scientific Reports,* 6.

Acknowledgements:

The authors acknowledge grant support from the NIH, UC TRDRP, M. Cook Chair, and fellowship support from the NIH and NSF.

Author:

Caylin M. Colson

Contact Address:	**340 Hearst Mining Building** **University of California, Berkeley** **Berkeley, CA 94720**
Email:	**caylin.colson@berkeley.edu**

Abstract Title:

Surface protein targeted molecular imaging approach for tracking white blood cells to inflammation using Magnetic Particle Imaging (WBC-MPI)

Authors:

K. L. Barry Fung[1,2]*, Prashant Chandrasekharan[2], Weiwen Cui[2], Xinyi Y. Zhou[1], Zhi Wei Tay[1], Caylin Colson[1], Elaine Yu[1], Quincy Le Huynh[3], Chinmoy Saayuja[3], Benjamin D. Fellows[2], Yao Lu[2], Steven M. Conolly[2,3]

Institution:

[1]UC Berkeley-UCSF Graduate Program in Bioengineering
[2]Department of Bioengineering, UC Berkeley
[3]Department of Electrical Engineering and Computer Sciences, UC Berkeley

Abstract:

Magnetic particle imaging (MPI) is a tracer imaging modality that detects superparamagnetic iron oxide nanoparticles (SPIOs). Recently, MPI has shown promise for sensitive (~200 cell), long term tracking of stem cells [1,2]. White blood cell (WBC) tracking has traditionally allowed for the clinical diagnosis of inflammation and is ordered in cases of fever-of-unknown-origin [3,4]. Recently, antibody based immunotherapeutic approaches have been developed to selectively modulate immune cells, e.g. for cancer treatment [5].

Objective: We developed the first *in vivo* approach to label and track neutrophils with MPI. The Ly6 family of glycosylphosphatidylinositol-linked proteins has been implicated in neutrophil migration and recruitment. Anti-Ly6 antibodies have been used at high concentration in mice to deplete neutrophils from circulation [5]. Fluorescent conjugated Anti-Ly6 antibodies are also used to track neutrophils [6]. We utilized Anti-Ly6G antibodies conjugated to SPIOs for *in situ* labelling and tracking of neutrophils in mice.

Methods: Inflammation was induced in a C57BL6 mouse (7-8 wks) by injecting lipopolysaccharide (LPS) (O111:B4, 50 ug) in the right thigh. The biodistribution was evaluated after i.v. injection of Anti-Ly6G antibody (IgG1, REA526 clone, Miltenyi Biotec, GmBH) SPIOs (6-6.5 mg Fe/kg, ~40 ug of protein/mouse) using a 6.3 T/m field-free line MPI scanner (field-of-view = 10.1 × 4.7 cm^2, t_{scan} = 15 min). The contralateral side of the mouse was used as control. The particles were also injected in a separate cohort of healthy C57BL6 mice and scanned. The inflamed mice had neutrophil activity validated with a bioluminescence scan using an i.p. injection of luminol (XenoLight RediJect Inflammation Probe, Perkin Elmer), imaged in an IVIS Lumina (Xenogen, Perkin Elmer) [7]. A high boost-filter was applied the MPI scansto improve conspicuity. Separately, the Anti-Ly6G SPIOs were magnetically characterized using a vibrating sample magnetometer, transmission electron microscope and arbitrary wave relaxometer [8], and compared to ferucarbotran (VivoTrax, Magnetic Insight), a common MPI tracer.

Results: SPIO characterization is shown in Fig 1, and shows improved performance in both resolution and signal per g Fe as compared to ferucarbotran, a common MPI tracer. 24-hr post i.v. injection, MPI images (Fig 2A) showed Ly6G tracer distribution in organs of the reticuloendothelial system (liver, spleen, as well as cranial, lower limb, and pelvic bone marrow) in healthy mice. These results concur with the delayed distribution of labelled WBCs in In111 scans shown in Fig 2C [9]. Fig 2B is an MPI image in which the mouse's right flank is inflamed, and tracer accumulation at the inflamed site appears with high contrast. This image and inflammation was validated with our luminol based images (Fig. 2D).

Conclusion: We performed the first WBC tracking MPI study targeting a surface specific ligand on neutrophils and observed homing of labelled neutrophils to inflamed sites. This zero-radiation approach can be invaluable for *in situ* labelled WBC scans for inflammation and infection, as well as the optimization of antibody-based cancer immunotherapies.

References:

[1] B. Zheng et al., *Nature Scientific Reports* 5, 2015.
[2] B. Zheng et al., *Theranostics* 2016.
[3] Lewis SS, et al, *Open Forum Infectious Diseases*. 2014;1(2):ofu089.
[4] Becker W., *European Journal of Nuclear Medicine*. 1995;22(10):1195-211.
[5] Bucher, K., F. et al. *J Leukoc Biol* 98(3): 365-372
[7] Tseng and Kung *J Vis E* 2013;
[8] Tay et al. *Sci Rep* 2016
[9] Love, C. et al, *Journal of Nuclear Medicine Technology* 32(2): 47-57.

Acknowledgements:

The authors would like to acknowledge help from the Electron Microscopy Lab at UC Berkeley for assistance with sample preparation and TEM imaging. The authors also thank the Salahuddin lab at UC Berkeley for access to their VSM. Funding support comes from NIH grants R01 EB019458 and EB024578, UC TRDRP grant 26IP-0049, Montford Cook Chair, and the UC Discovery Award, as well as from support from the Craven Scholarship from UC Berkeley BioE and the NSERC PGS-D for this work.

Author:

K. L. Barry Fung

Contact Address:	**340 Hearst Memorial Mining Building** **Berkeley, CA** **94720**
Email:	**barry.kl.fung@berkeley.edu**

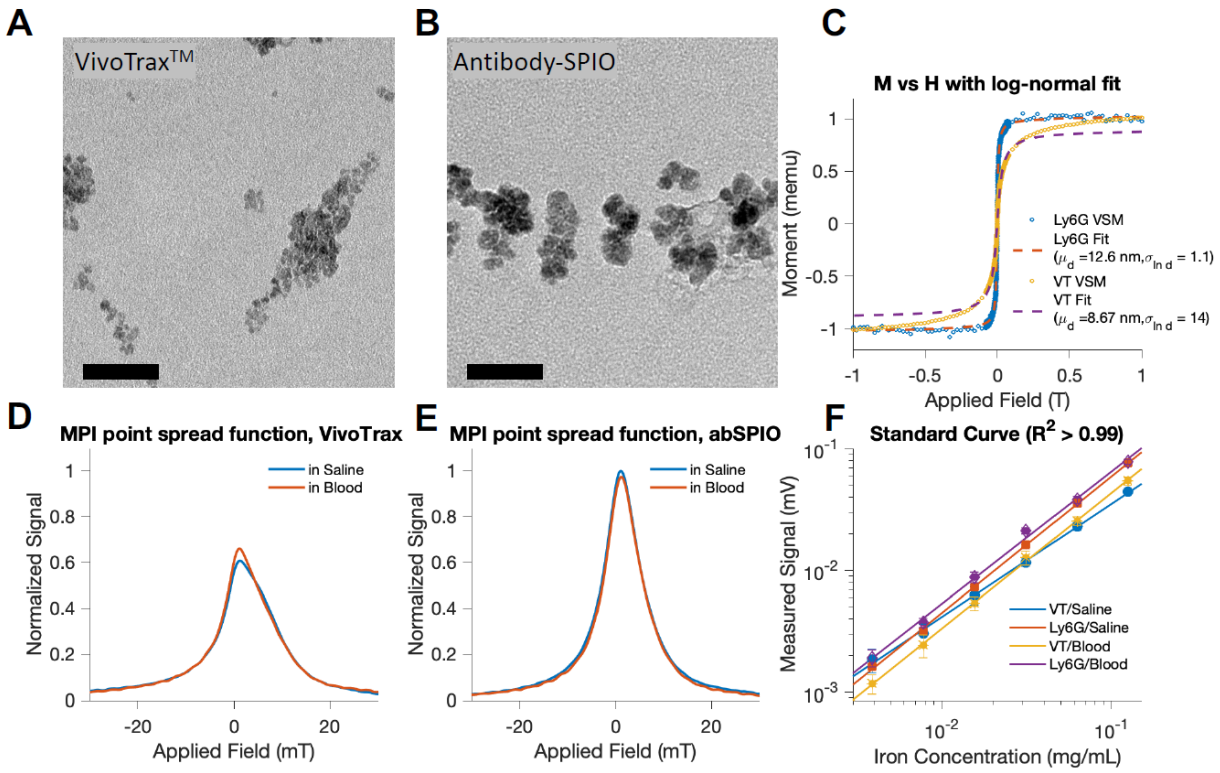

Figure 1: Representative transmission electron microscopy (TEM) images (scale bar = 50 nm) were taken of both **(A)** VivoTrax (VT) with core diameter = 5.4 ± 1.4 nm and **(B)** Anti-Ly6 SPIOs (abSPIO) with core diameter = 14.0 ± 2.6 nm. **(C)** The magnetization curve of VT and the abSPIOs as measured in a vibrating sample magnetometer was fit to a log-normal diameter distribution (abSPIO diameter mean 12.6 nm, with log-normal standard deviation of 1.1, and VT diameter mean 8.6, log-normal standard deviation of 14). We used a homebuilt relaxometer to measure the MPI point spread function (PSF) of **(D)** VT and **(E)** abSPIOs in saline and in blood, normalized to the maximum MPI signal per g Fe from both particles. Note the solvent-dependent blur in the PSF of VT in comparison unchanging behaviour of the abSPIOs, as well the abSPIOs superior full width half max and signal. **(F)** A standard curve of MPI signal was taken versus iron concentration for all particles in mouse blood and in saline. Both particles show linearity with concentration ($R^2 > 0.99$). VivoTrax showed significant ($p < 0.0001$) change in sensitivity (V/g), while the abSPIO did not ($p > 0.5$).

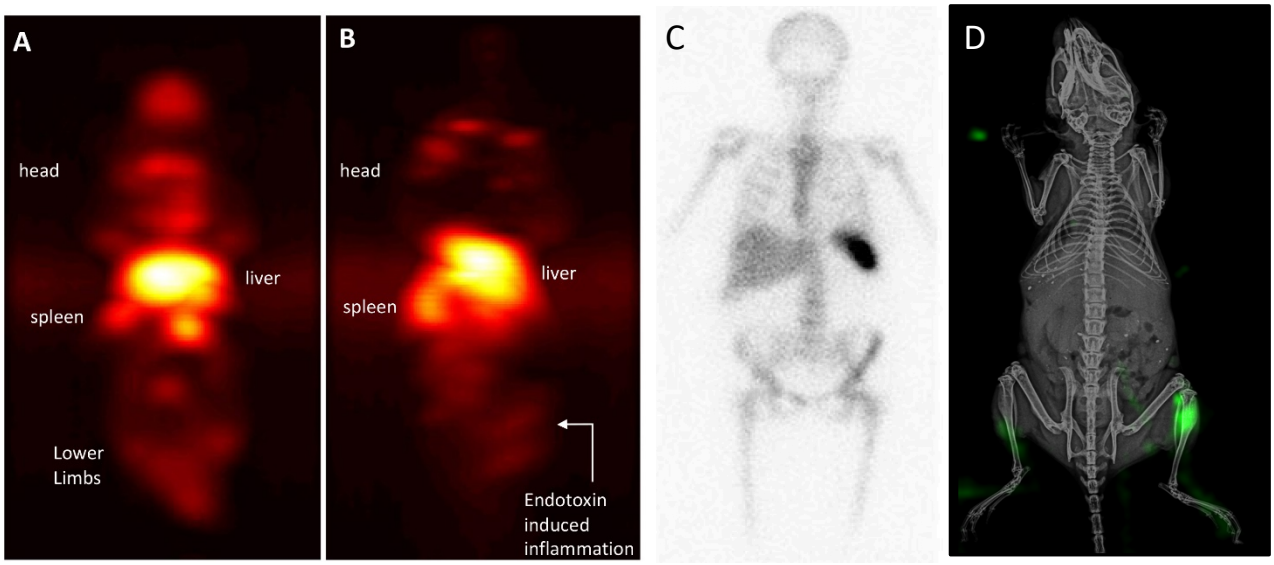

Figure 2: MPI images of *in situ* labeled neutrophils using anti-Ly6G iron oxide tracers and reference images from other modalities. (A) The tracer signal reveals the distribution of neutrophils in the myeloid cells of the bone marrow, and the RES organs of liver and spleen. **(B)** MPI images of a C57Bl6 mouse with inflamed right flank. Images 20 hour post anti-Ly6G tracer administration revealed the site of inflammation with high contrast – note the asymmetric signal in the flank of the mouse. **(C)** A healthy human WBC scan for comparison with (A) – note the uptake in the organs of the reticuloendothelial system (bone marrow, liver, spleen) (adapted from Love and Palestro *J. Nucl. Med. Tech.* 2004) **(D)** A bioluminescence image of an inflamed mouse with an i.p injection of luminol, a marker of neutrophil myeloperoxidase activity, co-registered to a representative x-ray. Note the strong luminescence in the inflamed right flank, similar to (B).

Title: Novel-View X-ray Image Generation by Deep Learning through Multi-Domain Image Translation

Author: Liyue Shen, Wei Zhao, Lei Xing

Purpose: X-ray imaging encodes the high-dimensional information of internal anatomic structure through the projection process over the 3D imaging subject. Here, we propose a data-driven deep-learning method for generating novel X-ray images in different view angles without 3D image supervision across different patients.

Methods: We develop a multi-domain image translation model to synthesize novel-view X-ray images from the given a single or two view(s), where each view is regarded as one image domain. Specifically, our framework consists of three modules: 1) Domain-shared encoder: encode anatomic information shared by X-ray images from different view angles; 2) Domain-specific encoder: encode information exclusively included in X-ray images from different view angles; 3) Generator: synthesize novel-view X-ray images by combining the domain-shared and domain-specific information learned from encoders. For evaluation, we conduct experiments to synthesize 15-view projections from 1 or 2 views on a dataset containing 1018 lung images, where 80% and 20% of the data are used for training and testing respectively. The X-ray images are digitally produced from CT images using geometry consistent with a clinical on-board cone-beam CT system.

Results: We deploy the trained model on the held-out testing set and compare the results with ground truth. For 1-to-15 view generation, the average MAE / RMSE / SSIM / PSNR values over all testing data are 0.026 / 0.146 / 0.929 / 27.098, respectively. For 2-to-15 view generation, the indices are found to be 0.023 / 0.130 / 0.938 / 28.264. The results show the proposed model can generate novel-view X-ray images close to the targets although the anatomic structures of different patients contain a large variance. Furthermore, the model trained on lung images is deployed on pancreas images and also produces promising results.

Conclusion: We present a deep-learning model for novel-view X-ray image generation across different patients. The proposed model may further contribute to more challenging research problems or practical medical applications, such as few-view CT reconstruction.

Innovation/Impact: We consider this study to be innovative because, for the first time, we propose to formulate the novel-view X-ray image generation problem as a multi-domain image translation problem, by regarding each view-angular X-ray image as one image domain. The proposed method is essentially different from previous approaches, since it learns the encoders to extract and disentangle the domain-shared underlying anatomy information and domain-specific view-dependent information from images in different view angles through a data-driven deep learning approach. Furthermore, we validate the robustness and generalizability of the proposed method across different organ cites. We deploy the model trained on lung X-ray images to pancreas X-ray images, and find it produces promising novel-view X-ray images as well. This work opens new opportunities for numerous practical applications and may revolutionize the future X-ray CT imaging systems.

Key results: Through the data-driven training process, we train the proposed model with 815 lung X-ray images and deploy on the held-out testing set of 203 lung X-ray images and 20 pancreas X-ray images. The results strongly demonstrate that our model is capable of generating high-quality X-ray images in novel view angles across different patients given only a single or two view projection(s). Figure 1 shows the proposed deep learning framework for X-ray image generation. Figure 2 shows results of two lung testing samples to generate 15 novel-view X-ray images (evenly distributed around a 360-degree circle) from 1 or 2 view(s). Figure 3 shows the inference results of two pancreas testing samples. Note that there is not any pancreas sample in training data. As illustrated in these figures, the generated X-ray images closely resemble the target images, indicating the potential of the proposed data-driven method for novel-view X-ray image generation across different patients given only ultra-sparse views.

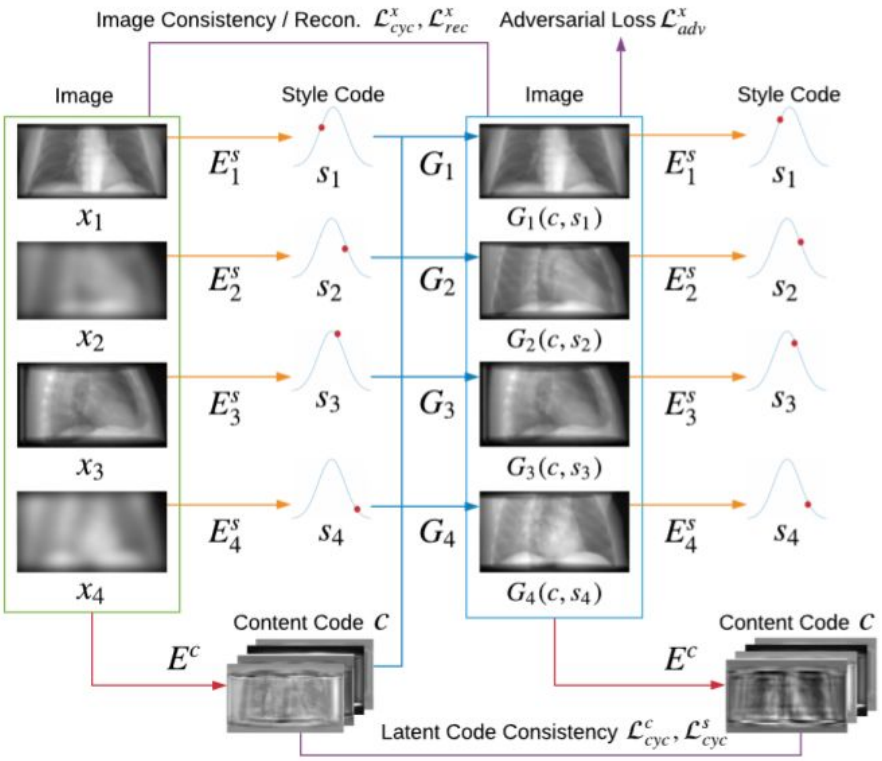

Figure 1. Overview of the proposed X-ray image generation network through multi-domain image translation. Two out of four domain images (x1 and x3) are given as inputs in this example. Our model contains a domain-shared content encoder (red lines), domain-specific encoders (orange lines) and image generators (blue lines). A variety of losses are adopted (burgundy lines), i.e., image and latent code consistency loss, adversarial loss and reconstruction loss for the generated X-ray images.

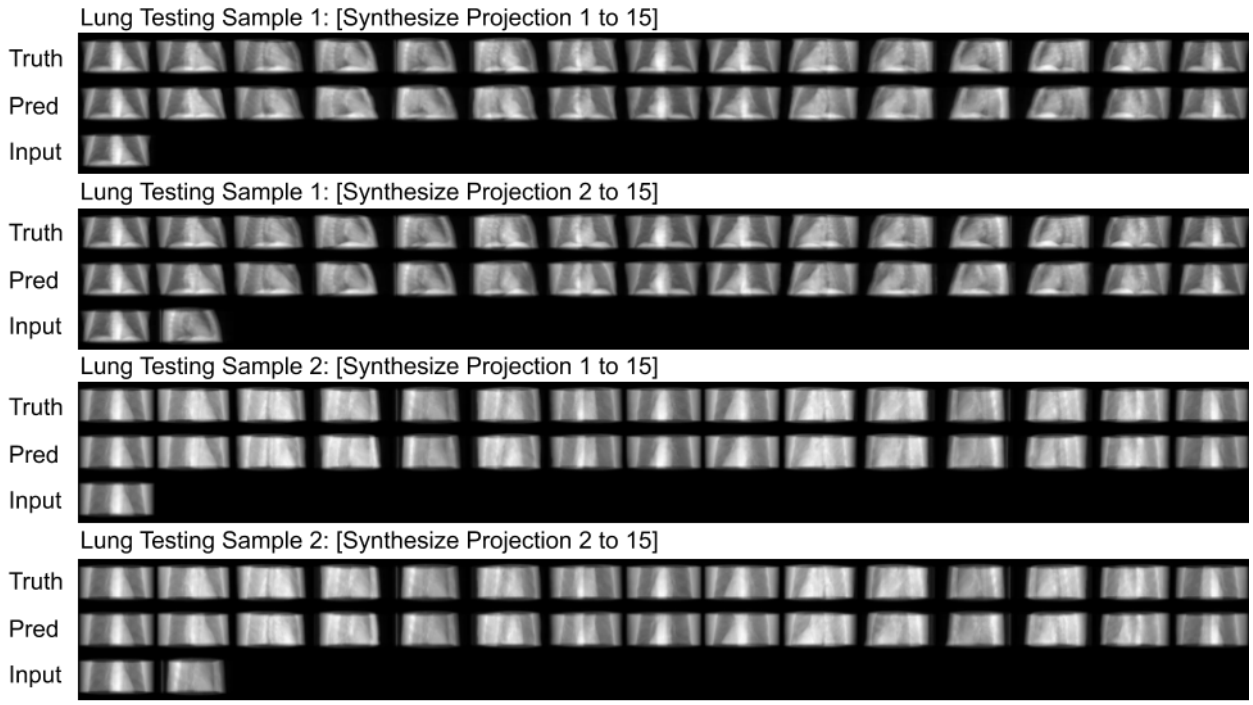

Figure 2. X-ray image generation results of two lung testing samples. Ground-truth and predicted novel-view X-ray images from 15 view angles when 1 or 2 projection(s) are inputted.

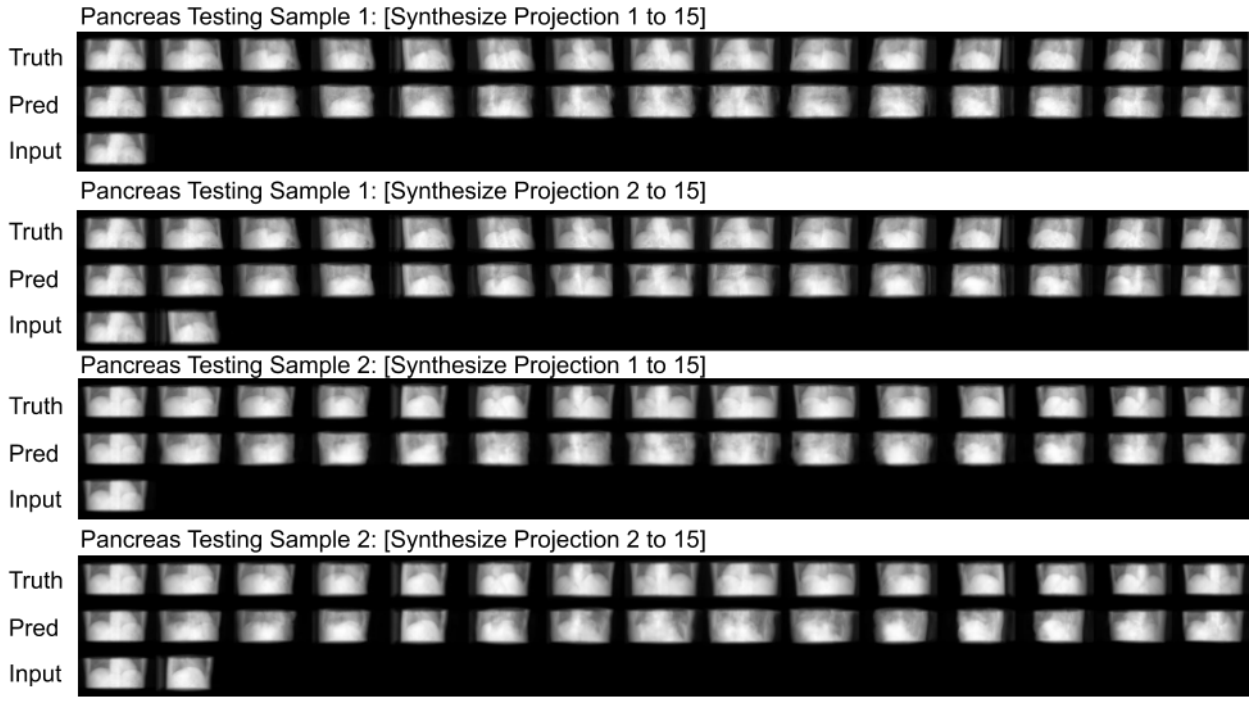

Figure 3. X-ray image generation results of two pancreas testing samples. Ground-truth and predicted novel-view X-ray images from 15 view angles when 1 or 2 projections are inputted.

A feasibility study of Time of Flight Computed Tomography

Ignacio O. Romero, Changqing Li*

Department of Bioengineering, University of California, Merced, Merced, CA 95343, USA.
*Corresponding: Changqing Li (cli32@ucmerced.edu)

Abstract:

Cone beam computed tomography (CBCT) has been investigated as a potential candidate to improve breast imaging. CBCT allows for three-dimensional imaging of the breast without compression. The CBCT images allow for complete visualization of the breast with enough spatial and contrast resolution for detection of masses at a radiation dose similar to conventional mammography. However, clinical trial results have shown no significant improvement in differentiating malignant from benign lesions compared with digital mammography.

Unlike conventional x-ray sources, free electron laser (FEL) produces monoenergetic x-rays from a process known as inverse Compton scattering. The FEL x-rays have quasi-monochromatic characteristics, tunable energy, super short pulse, and coherence. These features make this new type of x-ray source attractive for biomedical imaging. The super short x-ray pulse from FEL makes it possible to perform time of flight (TOF) computed tomography (CT) imaging. In TOF CT imaging, each TOF detector pixel only accepts an x-ray if the flight time is within the data acquisition time limit of that pixel. This allows for the rejection of most scattered x-ray photons which improves the CNR. In addition, the quasi-monochromatic x-rays in TOF CT diminish the beam hardening artifacts further increasing the CNR. The FEL allows us to tune the x-ray energy to image breasts with different densities.

We present a TOF CBCT simulation study performed with GATE (GEANT4 Application of Tomographic Emission). GATE software versions 8.0+ include the newly featured TOF measurement of each detected photon. In this work, we simulated a cylindrical water phantom with two spine bone targets. We removed the scattering photons from the total photon counts using the TOF information. We assume the detector time resolution was varied from 10 to 1000 picoseconds (ps). Our results show that the CNR is improved two times when the TOF CT has a time resolution of 10 ps. At 100 ps resolution, a 1.4 times improvement is seen in the CNR. We are currently simulating a breast-like phantom imported from the VICTRE software and will present results soon.

X-ray luminescence imaging for small animals

Michael C Lun[1], Wenxiang Cong[2], Md. Arifuzzaman[3], Meenakshi Ranasinghe[3], Sriparna Bhattacharya[4], Jeffery Anker[3,5], Ge Wang[2], and Changqing Li[1*]

[1]Department of Bioengineering, University of California, Merced, Merced, CA 95343, USA.
[2]Department of Biomedical Engineering, Biomedical Imaging Center, Center for Biotechnology and Interdisciplinary Studies, Rensselaer Polytechnic Institute, Troy, NY 12180, USA.
[3]Department of Chemistry, Clemson University, Clemson, SC 29634, USA.
[4]Clemson Nanomaterials Institute, Department of Physics & Astronomy, Clemson University, Clemson, SC 29634, USA.
[5]Department of Bioengineering, Center for Optical Materials Science and Engineering Technology
(COMSET), and Institute of Environment Toxicology (CU-ENTOX), Clemson University, Clemson, SC 29634, USA.
*Corresponding: Changqing Li (cli32@ucmerced.edu)

Abstract:

X-ray luminescence imaging has emerged for about one decade and combines the strengths of conventional x-ray imaging (high spatial resolution) and optical imaging (high measurement sensitivity). Specifically, x-ray luminescence computed tomography (XLCT) imaging has been studied and has potentials to become a powerful molecular imaging tool for small animals. There are typically two x-ray beam geometries utilized for XLCT imaging, namely the narrow x-ray beam based XLCT imaging which can obtain a high spatial resolution, even at significant depths, due to the precise spatial encoding of the x-ray beam in the reconstruction algorithm, and the conical beam based XLCT imaging which can obtain a very fast measurement time at the cost of a degraded spatial resolution. We have primarily focused our efforts towards the improvement of the narrow x-ray beam based XLCT imaging. We recently have proposed to use a polycapillary lens to generate a fine x-ray beam with a high x-ray photon flux to perform XLCT imaging. In this work, we demonstrate the potential of the focused x-ray beam based XLCT imaging in imaging a euthanized mouse and show that the distribution of an embedded phosphor contrast agent could be reconstructed with high precision. We are also developing a small animal dedicated focused x-ray luminescence tomography (FXLT) imaging system which also incorporates a microCT scanner in a single imaging system. We will show the designed imaging system as well as the current progress of the build inside our laboratory. In addition, we are working with collaborators to develop and synthesize biocompatible nanophosphors with distinct x-ray luminescence spectra to perform multi-color XLCT imaging with our designed imaging system. Lastly, we are currently developing a deep learning based XLCT reconstruction algorithm to reduce the number of projection views and x-ray beam translations with help from collaborators. A data synthesis method of projection views from measured few-view data based on deep learning is proposed to significantly enhance the quality of the XLCT image reconstruction.

FLASH irradiation can spare *in vitro* multicellular spheroids by rapid radiolytic depletion of oxygen

S. Khan[†], M. Bassenne[†], J. Wang, R. Manjappa, D. Y. Breitkreutz, L. Xing, B. W. Loo Jr, and G. Pratx*
Department of Radiation Oncology, Stanford University, Stanford, CA
Presenting author: drskhan@stanford.edu; *Corresponding author: pratx@stanford.edu

Purpose: The differential response of normal and tumor tissues to ultra-high dose rate radiation (FLASH) has raised new hope for treating cancer patients but the mechanism remains elusive. One leading hypothesis is that FLASH radiochemically depletes oxygen from irradiated tissues faster than it is replenished through diffusion. The purpose of this study is to investigate these effects within hypoxic multicellular tumor spheroids, through simulations and experiments.

Materials and Methods: Physicobiological equations were derived to model (i) the diffusion and metabolism of oxygen within spheroids; (ii) its depletion through reactions involving radiation-induced radicals; and (iii) the increase in radioresistance of spheroids, modeled according to the classical oxygen enhancement ratio and linear-quadratic response. These predictions were then tested experimentally in A549 spheroids exposed to electron irradiation (0-20 Gy, 16 MeV) at conventional (0.01 Gy/s) or FLASH (90 Gy/s) dose rates. Conventional 2D-cultured cells were irradiated as a negative control. Clonogenic survival, cell viability, and spheroid growth delay were scored post-radiation.

Results: The formation of a substantial hypoxic core in unirradiated tumor spheroids is predicted by numerical simulations and confirmed by fluorescence microscopy. Upon FLASH irradiation, this hypoxic core transiently increases in volume, engulfing and thereby radio-protecting the non-hypoxic cells. In contrast, oxygen diffusion easily replenishes the oxygen lost during slow conventional irradiation. Experimentally, clonogenic survival was around 3-fold higher in FLASH-irradiated spheroid compared to conventional irradiation, but no difference was observed for well-oxygenated 2D-cultured cells. This

differential survival is consistent with the predictions of the computational model. The corresponding dose-modifying factor of FLASH irradiation was 0.7 at 10 Gy.

Conclusion: A549 tumor spheroids can be used as models to study FLASH irradiation *in vitro*. The improved survival of tumor spheroids to FLASH radiation confirms that ultra-fast radiochemical oxygen depletion and its slow replenishment are critical components of the FLASH effect.

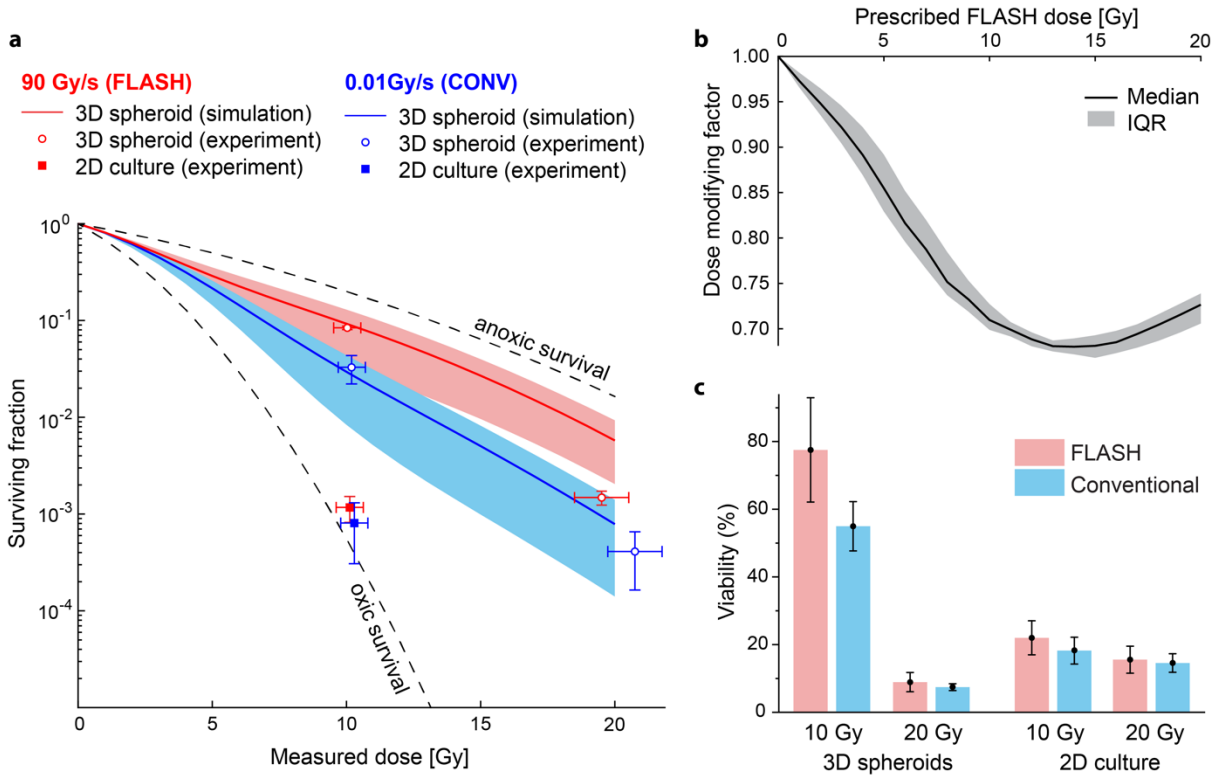

Figure 1: Response of A549 cells to conventional and FLASH irradiation. (a) *Dashed lines*: predicted survival of cells in anoxic and oxic conditions, respectively (LQ model; OER = 3). *Solid lines*: simulated average cell survival within the entire spheroid from conventional (blue) and FLASH (red) radiation. The shaded area represents the interquartile range. *Markers:* Experimentally measured clonogenic survival of cells in 3D spheroids (○) and 2D culture (■) for FLASH and conventional dose rate. Vertical error bars represent standard deviation (n=3). Horizontal error bars represent 5% uncertainty for film dosimetry. 3D spheroids demonstrate 3-fold higher survival with FLASH than conventional radiation. 2D cell survival falls near the oxic curve irrespective of the radiation method. (b) Dose modifying factor for FLASH calculated at different prescribed doses. (c) Cell viability assay (CCK-8) for irradiated spheroids and 2D cultures. The overall viability of spheroids was higher with 10G y FLASH compared to 10 Gy conventional irradiation ($P<0.01$) but the other differences were not significant.

Lutetium Background Radiation in uEXPLORER Total-body PET Scanner: Applications and Challenges in Attenuation Correction

Negar Omidvari[1], Li Cheng[1,2], Edwin K Leung[1,3], Ramsey D Badawi[1,3], Jinyi Qi[1] and Simon R Cherry[1,3]

[1] Department of Biomedical Engineering, University of California, Davis, Davis, CA 95616, USA
[2] Department of Engineering Physics, Tsinghua University, Beijing 100084, China
[3] Department of Radiology, University of California, Davis, Medical Center, Sacramento, CA 95817, USA

Lutetium-based scintillation crystals, such as LSO (Lu_2SiO_5) and LYSO ($Lu_{1.8}Y_{0.2}SiO_5$), are the building blocks of all start-of-the-art commercial PET scanners, offering high density, high light output, and fast timing response. One concern with use of Lutetium-based crystals in PET scanners is their intrinsic radiation background. The source of this radiation is ^{176}Lu, which is abundant in 2.6% of natural occurring lutetium, and decays by beta emission with three prompt gamma-rays of 307, 202 and 88 keV. This background radiation increases the rate of singles events and rate of random coincidences, consequently, and becomes a more important issue at low activity levels. On the other hand, these background events can be utilized for detector calibration and quality control, as well as for PET attenuation correction (AC).

Using the 307 keV photons of ^{176}Lu as transmission source for PET AC, instead of CT, has already been studied in conventional short axial field-of-view (AFOV) scanners. In these scanners, the 307 keV transmission data is used together with the PET emission data, in Maximum likelihood reconstruction of attenuation and activity (MLAA) algorithms, to provide AC with sufficient quality. This requires about 10 min of transmission data in each bed position and high count-statistics in PET emission data. As the volume of crystals increases in a total-body PET scanner, utilization of the ^{176}Lu events becomes of a greater interest, as the scanner offers higher and more uniform sensitivity throughout the AFOV and possibility of a whole-body scan in a single bed position. This allows use of background radiation in standard clinical protocols with no increase in scan duration or radiation dose. Furthermore, the higher sensitivity sets the threshold for emission counts to a lower level. This becomes particularly beneficial in ultra-low dose pediatric scans (in which emission data has a low-statistic nature) or radiotherapy monitoring, requiring multiple follow-up scans, where additional CT dose can be avoided.

In this study, the ^{176}Lu background radiation of the uEXPLORER total-body scanner is characterized and utilization of the background events for AC is investigated in Monte-Carlo simulations of the scanner with a 3D whole-body XCAT phantom. Since the fraction of scattered and attenuated photons increase in oblique lines-of-response, attenuation maps have been reconstructed and compared in different cases, where scanner AFOV and acceptance angle are varied.

Laser-like x-ray sources for a new SRS/SBRT paradigm

E. Simiele, D. Breitkreutz, D. Capaldi, and L. Skinner

Purpose: Monte Carlo simulations of inverse Compton x-ray sources (ICS), which offer low divergence, monochromatic x-rays in the 50-200 keV range were performed. These sources have sharp penumbra and strong high-Z contrast enhancement, while providing depth-dose fall-off equivalent to Bremsstrahlung sources at 5-6 times higher kVp energies.

Methods: Simulations were performed using the egs brachy user code of EGSnrc to utilize low-energy photon variance reduction techniques. The ICS source divergence and spectra were obtained from the literature. Nominal photon energies of 80keV and 150keV were investigated. An energy of 80keV represents optimal gold dose-enhancement, and a bone dose-enhancement factor of 2.5-3 versus water. The 150keV energy provides less gold enhancement, but greater penetration (bone dose-enhancement 1.15). Simulations were performed in a 30x30x30cc water phantom including cortical-bone slabs placed at various depths. Further calculations include three test CT cases including brain and spine treatments performed for both the ICS and clinical 6MV photon beams.

Results: The ICS profiles have an extremely sharp fall-off (<0.1 mm wide) with a broad low-dose tail that starts at 5-30% of the dose on the central axis depending on depth and energy. Without adding gold-nanoparticles (GNP), the brain case gave comparable plan quality for the ICS calculations and 6MV. Adding 10mg/g of GNP to the target volume reduced the V12Gy of the normal brain volume by a factor 40 for 80keV versus 6MV. The Paddick conformity index also significantly improved for ICS calculations with GNP's compared to 6MV. Better plan quality was achieved in the spine cases where the dose-to-bone enhancement of the ICS beams enables better conformity and better spinal cord sparing compared to 6MV.

Conclusions: The sharp penumbra and preferential absorption of the ICS by high-Z materials indicates that inverse Compton x-ray sources could be useful for stereotactic radiosurgery that require steep dose gradients.

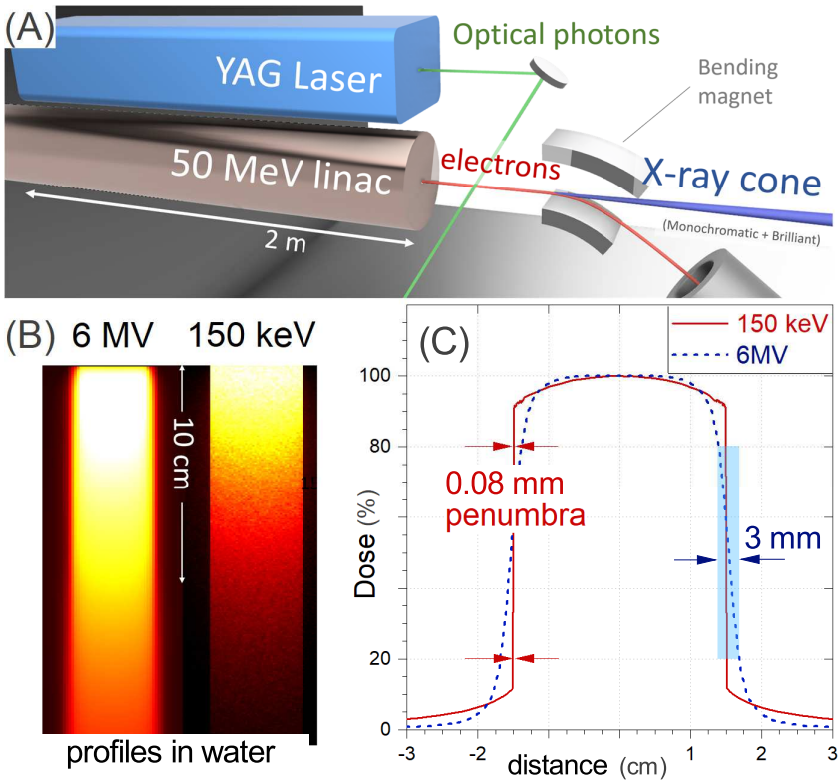

Figure 1: A) Schematic representing the process of generating an Inverse Compton keV photon source (ICS). Briefly, optical photons are injected into an interaction cavity with 50 MeV electrons where the optical photons are scattered from the high-energy electrons. The scattered photons exit the cavity with significantly more energy than the entering optical photons. The main benefits of ICS beams are the near monochromatic energy and extremely low divergence, which results in a high brilliance as compared to traditional kV and MV photon therapy sources. B) Dose profiles in water as a function of depth for a clinical 6 MV and a 150 keV ICS photon beam. C) 1D dose profiles from B) at 2 cm depth are shown for the two beams. The calculated 80-20 penumbra values are also indicated for the two beams and it is clear the intense brilliance of the ICS beam results in a sharp penumbra as compared to the clinical 6 MV beam.

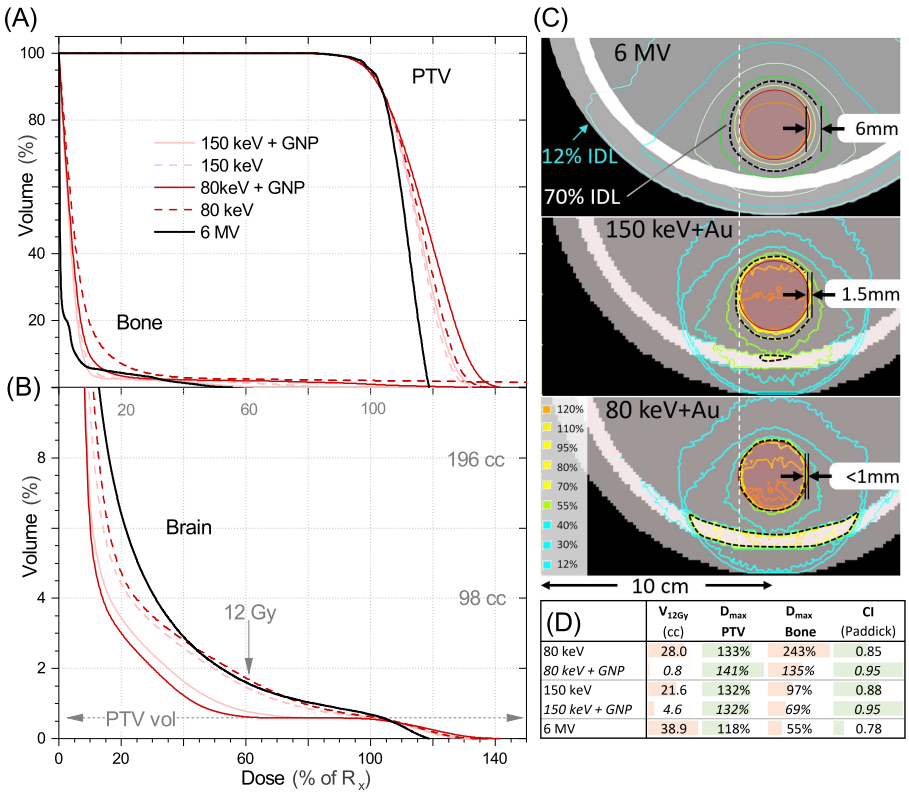

(D)

	V_{12Gy} (cc)	D_{max} PTV	D_{max} Bone	CI (Paddick)
80 keV	28.0	133%	243%	0.85
80 keV + GNP	*0.8*	*141%*	*135%*	*0.95*
150 keV	21.6	132%	97%	0.88
150 keV + GNP	*4.6*	*132%*	*69%*	*0.95*
6 MV	38.9	118%	55%	0.78

Figure 2: A) and B) are example dose volume histograms (DVH's) for a simple partial-arc plan for a single brain metastasis with corresponding axial slices shown in C). The planning target volume (PTV) consisted of a 2 cm-diameter sphere inside a 20 cm diameter spherical "head", which contained a 6 mm thick bone "skull". The 6 MV plan was calculated with Varian Acuros using a C-series linear accelerator beam model. The ICS beams were calculated with the egs brachy user code of the EGSnrc Monte Carlo radiation transport code. Five calculations are shown across three photon energies: 80 keV, 150 keV, and 6 MV (clinical beam). All calculations were normalized to 95% coverage of the PTV by the 20 Gy prescription dose. The two keV energies were simulated with and without gold nanoparticles present inside the target volume. Gold nanoparticles were not included in the 6 MV calculations as the physical dose enhancement was expected to be 1% compared to 30-90% for the keV beams at a concentration of 10 mg of gold per gram of brain tissue inside the target. For the slices shown in C) the "6 mm", "1.5 mm", and "<1 mm" are referring to the distance between the 70% and 110% isodose lines. The dashed black curves in C) indicate the 70% isodose line.

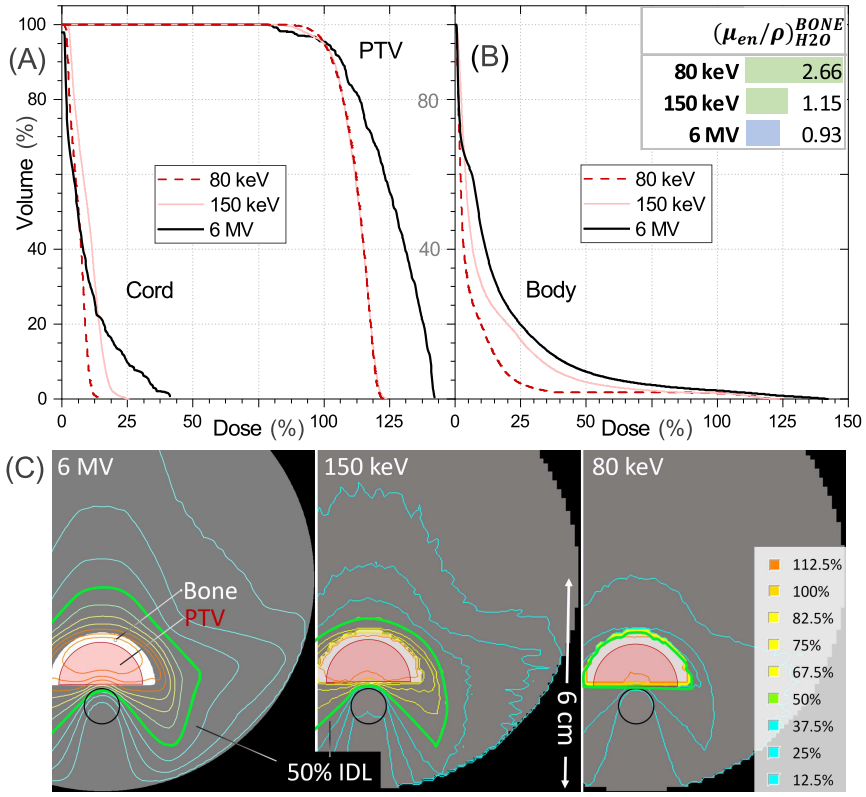

Figure 3: A) and B) are DVH's for a simple partial-arc plan on a phantom approximating a lumbar spine with corresponding axial slices shown in C). Specifically, a half-cylinder of ICRU 44 cortical bone was placed 3.0 cm deep inside a 12 cm diameter cylinder of water. The energies shown correspond to a 6 MV clinical beam, a 80 keV photon beam, and a 150 keV photon beam. Significant dose enhancement in the bone for the 80 keV condenses the 40-100% isodose lines to overlap within 1 mm. Milder dose enhancement is seen for the 150 keV energy. The sharper 80-20 penumbra of the keV beams also allows better sparing of the spinal cord (black contour). The combination of enhanced dose to bone and sharp penumbra from the ICS beams indicates these beams are well-suited for spine treatments where the cord is within 3 mm of the PTV.

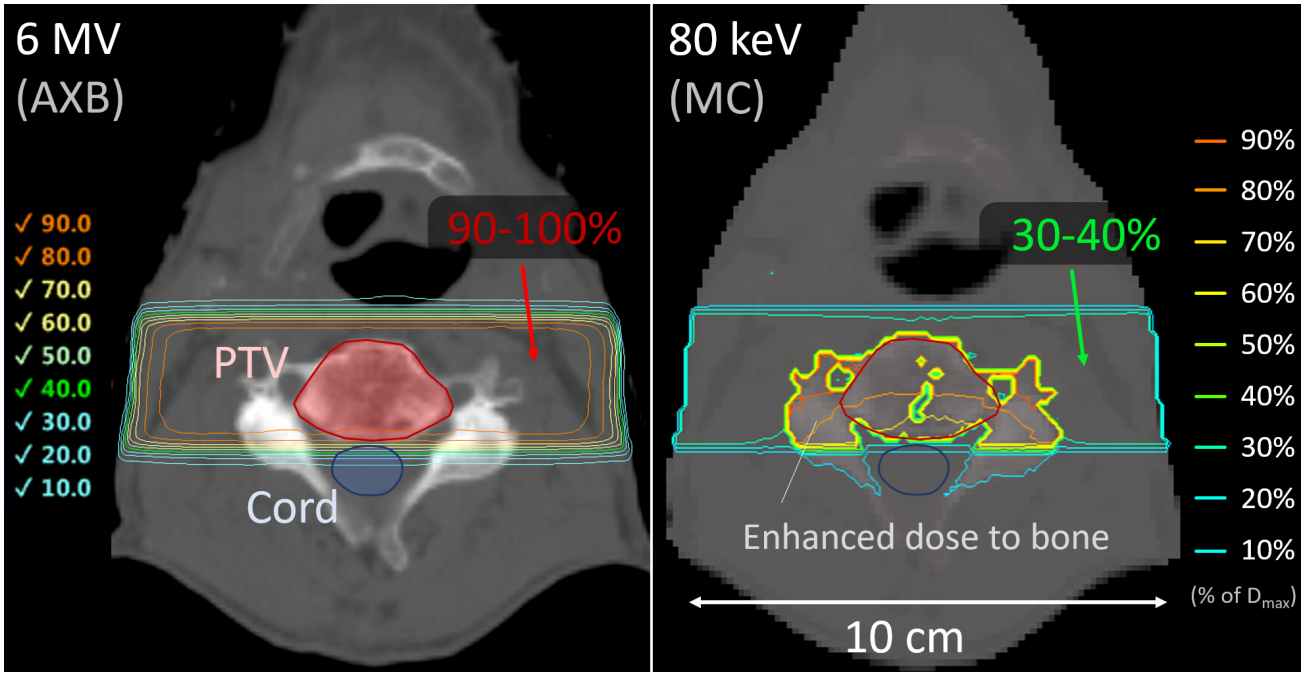

Figure 4: Example axial slices of the isodose lines from opposing lateral fields from the clinical 6 MV (left) and 80 keV (right) ICS beams for irradiation of a cervical spine target. Due to the strong absorption of the ICS photons in the bone through the photoelectric effect, the normal neck tissue was greatly spared compared to the comparable 6 MV plan. Furthermore, the sparing of the spinal cord was much greater with the ICS beam as compared to the 6 MV beam due to the sharp penumbra inherent to the ICS beams.

A more accurate assessment of pulmonary ^{18}F-FDG PET as an imaging biomarker for post-radiotherapy pulmonary toxicity through partial volume correction.

Abstract

PURPOSE:

Evidence indicates an association between increased ^{18}F-FDG uptake in the lungs before radiotherapy (RT) and pulmonary toxicity after RT. However, there are conflicting data on the effect of spatial overlap between lung regions with increased ^{18}F-FDG uptake and dose. Correction for partial volume averaging due to air within each voxel may allow a better localization of increased uptake regions. In this study we quantified the effect of tissue-fraction correction in ^{18}F-FDG-PET in lung cancer patients.

METHODS:

Patients with stage I and III non-small cell lung cancer underwent standard-of-care staging ^{18}F-FDG-PET with low-dose CT prior to RT. CT images were resampled to match the resolution of PET images, and regions of interest (ROIs) were generated for both lungs so as to only include voxels with values between -1024 and -600 Hounsfield units (HUs). PET images were then masked by those ROIs and each voxel value was reassigned an ^{18}F-FDG uptake corrected for its tissue-fraction estimated using HUs in the corresponding CT. Finally, the original and corrected PET images were compared using the Spearman's rank voxel-wise correlation coefficient.

RESULTS:

The Spearman's rank voxel-wise correlation between the original and tissue-fraction corrected PET images ranged from mild (0.436) to strong (0.929) (standard deviation: 0.218) for the whole lung, where the correlations for the right and left lungs were similar for each patient. Two patients who also had chronic obstructive pulmonary disease (COPD) had the lowest Spearman rank correlations (0.436 and 0.498), which can be explained by spatial heterogeneity of lung tissue fractions in those patients.

CONCLUSIONS:

The effect of tissue-fraction correction in pulmonary ^{18}F-FDG-PET varied widely between the five lung cancer patients, suggesting that the spatial location of high uptake regions may change after correction in some cases. This correction method may improve the predictive value of ^{18}F-FDG-PET for pulmonary toxicity following RT.

Continuous Generation of Volumetric Images During Radiation Therapy Using a 4DCT-Based Patient-Specific Motion Model, Periodic kV Imaging and a Continuous External Respiratory Surrogate Signal

April 24, 2020

Purpose

During radiation therapy, respiratory motion can lead to inter- and intra-fraction variations in patient anatomy, which may result in discrepancies between planned and delivered dose. Continuous knowledge of a patient's three-dimensional anatomy is required to fully assess the motion's dosimetric impact, and would enable treatment adaptation to account for delivered dose deviations. However, current clinical imaging techniques do not provide sufficient information to fully reconstruct 3D anatomy in real time on clinical linear accelerators. We present a technique for generating continuous volumetric images during radiotherapy using a 4DCT-based motion model, periodic kV imaging and a continuous external respiratory surrogate signal.

Methods

A patient-specific motion model is constructed by performing principal component analysis on deformation vector fields produced from deformably registering the phases of the patient's pre-treatment 4DCT scan. Using the on-board imager, kV radiographs are acquired every 3 seconds and used to determine the motion model components' weights. A multi-dimensional correlation model is established between the motion model and the external surrogate signal, enabling continuous volumetric image reconstruction between kV imaging time points. The algorithm performance was evaluated with 10 digital e**X**tended **CA**rdiac-**T**orso (XCAT) phantom datasets, enabling a comparison against a full 3D ground truth. The phantoms were programmed with measured 3D tumor motion traces and the measured external surrogate trace was used, thus incorporating realistic irregularities in breathing patterns and changes in internal-external correlation.

Results

The three-dimensional tumor positions are reconstructed with an average root mean square error of 1.47 mm, and an average 95^{th} percentile 3D positional error of 2.80 mm.

Conclusion

Through combining a 4DCT-based motion model, periodic kV imaging, and external surrogate information, this technique enables continuous 3D image generation on clinical accelerators without the additional dose of continuous kV imaging, and provides a new capability for treatment verification and calculating delivered dose in the presence of irregular respiratory motion.

Continuous Generation of Volumetric Images During Radiotherapy

Purpose & Detailed Methodology

When a patient undergoes radiotherapy treatment, its internal anatomy changes with time because of respiration, which becomes a source of discrepancies between the planned and the delivered treatment. Currently volumetric images can be generated from planar kV images, however the time interval between each kV image being acquired is large enough to introduce significant uncertainty in the delivered dose calculation. To improve the time resolution of the delivered dose calculation, we developed a technique that uses both an external respiratory surrogate and periodic triggered kV images in combination with a patient-specific motion model built from a pre-treatment 4DCT scan to perform continuous estimation of a patient's full 3D anatomy throughout the delivery of a radiotherapy fraction, thus allowing more accurate delivered dose calculation.

We use 4DCT volumetric images at different time points to generate deformation vector fields (DVF) with a demons based deformable image registration (DIR) algorithm. We perform principal component analysis (PCA) on the DIR generated DVFs to obtain a motion model.

A Forward Iterative Reconstruction (FIR) algorithm is then used to generate volumetric images from the planar kV images and a digitally reconstructed radiograph (DRR) of the reference CT volumetric image. A DRR of the reference volumetric image is generated. When using pre-treatment 4DCT images as the training set for the motion model, the reference DRR is compared to a planar kV image that is obtained during treatment. When using XCAT phantom images as the training set for the motion model, the reference DRR is compared to a DRR projection of a 3D XCAT phantom image which mimics an in-treatment kV image. The PCA weights are adjusted to deform the DRR of the reference volumetric image so that it matches the kV image (or the DRR projection of a 3D XCAT phantom image).

A correlation model is built between the PCA coefficients obtained from performing FIR and both the surrogate amplitude and velocity (figure 1). This allows the creation of new volumetric images at time-points where no kV images are available, to improve the delivered dose calculation.

The average 95^{th} percentile 3D error between correlation model-generated volumetric images and ground truth volumetric images was 2.80 mm, and the RMSE was 1.47 mm (figure 2).

Impact: Translating results from motion modeling research to clinical radiotherapy treatments for improved delivered dose calculation.

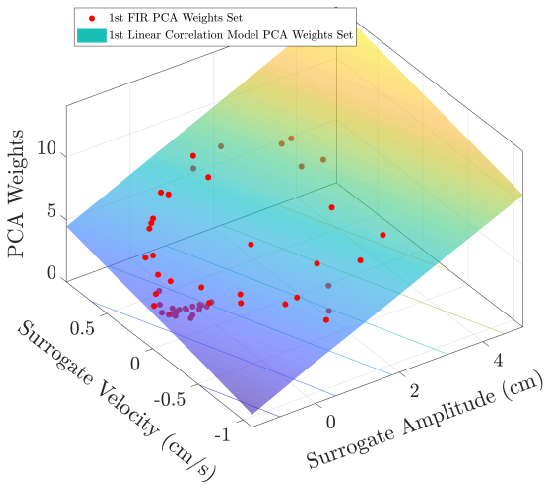

Figure 1: Correlation between PCA weights and surrogate amplitude and velocity.

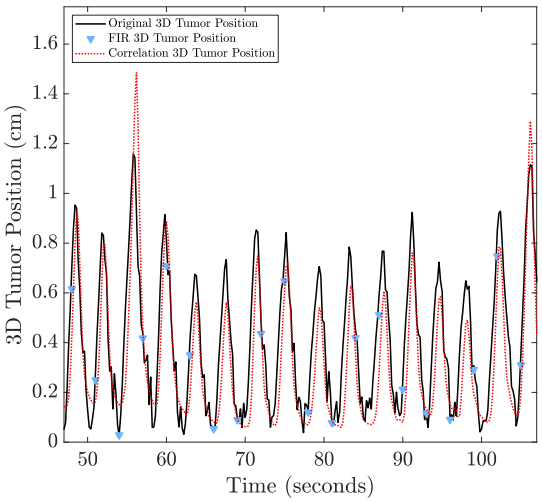

Figure 2: 3D tumor positions reconstruction with FIR, as well as with the correlation model.

Title: Reducing IMRT QA workload by 95% and keeping the same level of quality control

Authors: Tomi F. Nano[1], Martina Descovich[1], Emily Hirata[1], Yannet Interian[2] and Gilmer Valdes[1]

1. University of California San Francisco (UCSF), Department of Radiation Oncology
2. University of San Francisco (USF), Department of Data Science

Purpose: To reduce the maximum possible error (max-error) in a quality assurance (QA) program by using a novel machine learning (ML) algorithm for predicting QA plan passing rate that minimizes the max-error.

Methods: A total of 498 patient IMRT QA plans were measured using a commercial 2D diode array (Sun Nuclear's MapCheck®) and delivered on five isocentric linear accelerators. Passing rates were based on a tolerance of 3%/3mm local dose and distance-to-agreement. Each treatment plan was characterized by 78 complexity features. Two ML models were used to predict passing rate: (1) an ordinary least squares (OLS) linear model that minimize the mean of the expected error; and (2) Chebyshev minimax (MM) linear solution that minimizes max-error. An 80% training dataset was used for fitting and optimization, and a 20% testing dataset was used to compare predictions.

Results: Max-error of IMRT QA passing rate predictions was 7.6% for the OLS model and 3.0% for the MM model. The mean square error was, however, 1.4% and 2.8% for the OLS and MM models respectively. Following optimization and testing with hold-out sets (20% plans), the OLS and MM model max-errors were 7.0% and 3.8% respectively. To ensure that all plans have at least a 90% passing rate, all plans predicted to have 97.0% passing rate or lower (79 out of 497, 16.0%) would require QA using the OLS model. With the MM model, however, all plans predicted to be 93.8% or lower (24 out of 497, 4.8%) would require QA, resulting in more than a 3x reduction compared to the OLS model.

Conclusion: Efficient QA programs that ensure safe IMRT treatments require accurate identification of plans that are likely to fail QA criteria. Using Chebyshev minimax optimization, a 95% reduction of resources for IMRT QA can be achieved while meeting current passing criteria.

Rationale: Current machine learning methods for predicting IMRT quality assurance metrics minimize the average error over all plans. However, we care about minimizing the **maximum error** possible over all plans because one erroneous prediction for a single patient can result in a wrong decision regardless of low average error over the whole population. Our objective is to introduce Chebyshev minimax loss function as the natural selection for IMRT QA metrics that minimize the maximum error when predicting QA passing rate. Our proposed method will be compared to a typical linear model that use ordinary least-squares minimization.

Methods: Patient IMRT QA plans for 498 cases were recorded using a commercial 2D diode array and delivered on 5 linear accelerators and passing rates were determined based on 3%/3mm local dose/distance-to-agreement (DTA). Each plan was characterized by 78 features that describe plan complexity. We've developed an algorithm using Chebyshev minimax (MM) for comparison with ordinary least-squares error (OLS).

OLS minimization problem/solution are given below:

$$\text{minimize} \quad f_0(x) = \|Ax - b\|_2^2 = \sum_{i=1}^{k} (a_i^T x - b_i)^2.$$

$$\begin{array}{ll} \text{minimize} & \|Ax - b\|_2^2 \\ \text{subject to} & l_i \leq x_i \leq u_i, \quad i = 1, \ldots, n, \end{array}$$

Minimax problem and linear solution are given below:

$$\text{minimize} \quad \max_{i=1,\ldots,k} |a_i^T x - b_i|.$$

$$\begin{array}{ll} \text{minimize} & t \\ \text{subject to} & a_i^T x - t \leq b_i, \quad i = 1, \ldots, k \\ & -a_i^T x - t \leq -b_i, \quad i = 1, \ldots, k, \end{array}$$

where A is an MxN matrix with each row containing a plan (M plans) and each column its respective plan feature values (N features), x is a Nx1 matrix of coefficients in the linear model and b is an Mx1 matrix containing passing rate of each plan's IMRT QA.

Results: We compare MM and OLS linear models by using all of our data as training and prediction datasets. This is an ideal scenario that will allow us to demonstrate how Minimax method performs. All 498 cases were used to fit and predict with MM and LSE linear models. Figure 1 shows a histogram of the errors for each case using LSE (left) and MM (right) models. For the LSE model, the distribution of prediction differences has most cases errors close to zero and 10 cases with errors greater than 3% from actual passing rate. Whereas the MM model predictions have many cases with error +/- 2.7% but no cases greater than 3% error. The differences in the prediction differences between MM and LSE models demonstrates how minimizing the maximum reduces max error at the expense of greater mean error. For LSE model, the mean squared error is 1.39% and max error is 7.6%. For MM model, the mean squared error is 2.96% and the max error is 2.77%.

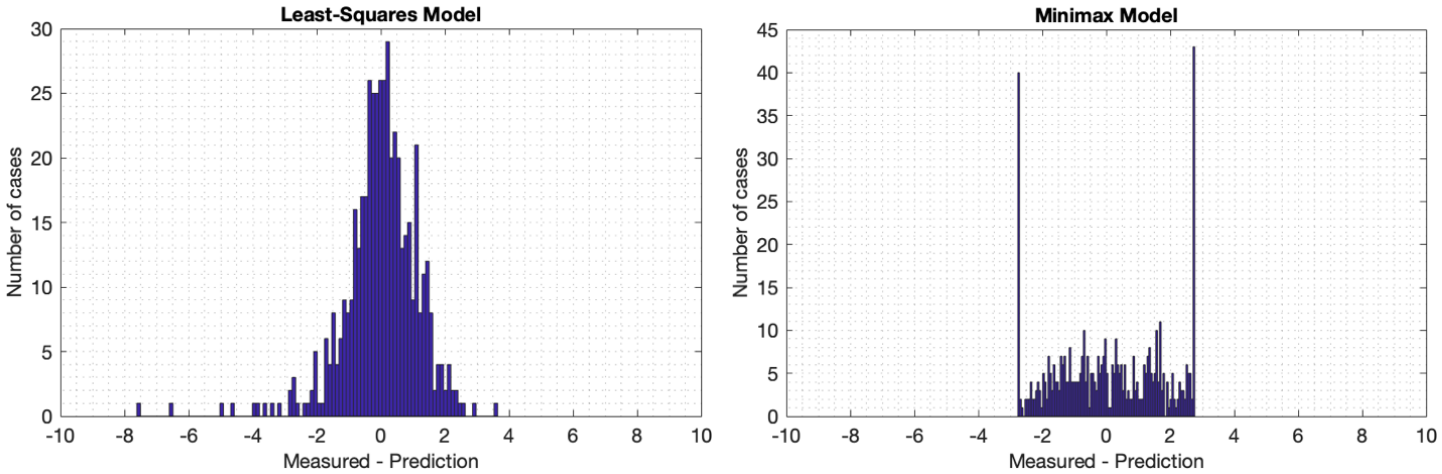

Figure 1. Differences in IMRT QA passing rate for 498 predictions using least-squares error (left) and minimax (right) minimization. Max error was 7.61% for LSE and only 2.77% for MM predictions. Lower max error with MM predictions comes with the expense of greater mean square error (1.39% and 2.96% with LSE and MM).

Figure 2 more clearly shows that MM model has no outliers (greater than +/-3%). Solid line indicates perfect match between actual passing rate and prediction, and dashed lines show +/- 3% difference thresholds. Additional data was generated using a Random Forrest model that was fit to our data to generate new observations from new features. New features were generated as a linear combination of measured features. A total of 10,000 cases were generated and this data was used for variance-bias analysis and regularization. We

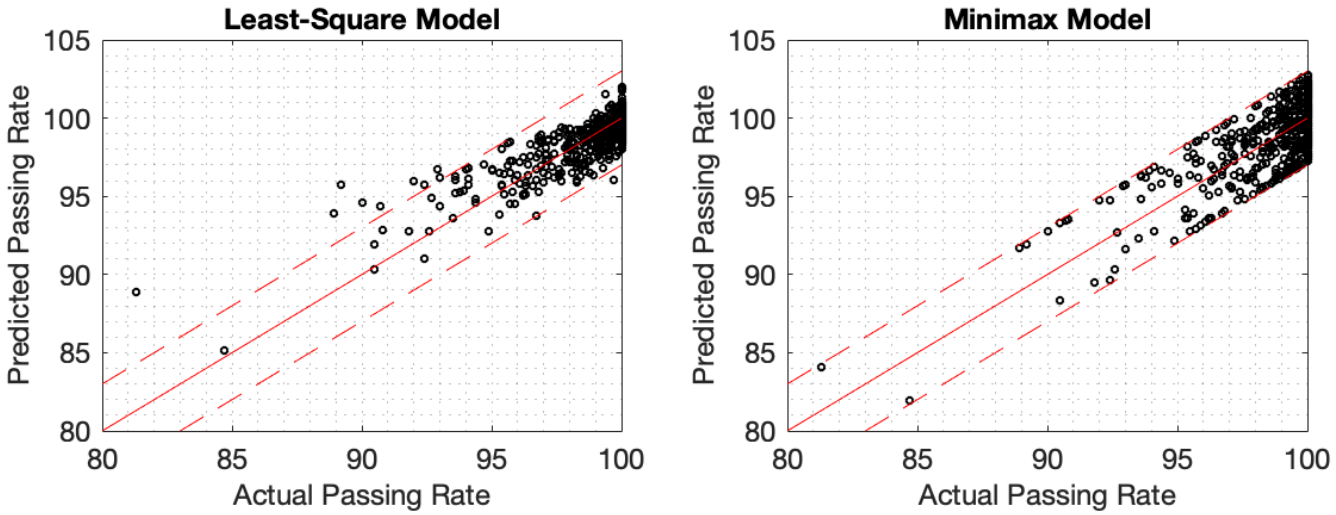

Figure 2. Predicted and actual passing rate for LSE (left) and MM (right) models. Solid line is perfect agreement and dashed lines are +/- 3%, showing that no plans pass this threshold with the MM model.

generated 10,000 cases for both training and testing datasets. For a given training dataset size, 100 models were fit and used to predict on 10,000 test case. Greater variability was seen in testing dataset with MM model. Minimax with Lasso light regularization. A 95/5% split was used for training and test. 25 trails averaged to show mean and standard deviation for different lambda values. Using log(lambda) = -7.5, and performing bias-variance analysis for Minimax again. We used 80% of the data to train both LSE and MM models and tested them each on the remainder 20% of the data. As shown in Figure 3, LSE max error for prediction overestimating measurement is 7%, meaning we need to QA all plans having 97% passing rate or lower (79 out of 497, 16.0%) to ensure plans will have 90% or more passing criteria. Minimax prediction error is 4%, meaning we need to QA all plans 94% or lower (24 out of 497, 4.8%) which is 1/4th of the amount that you would need to do with LSE.

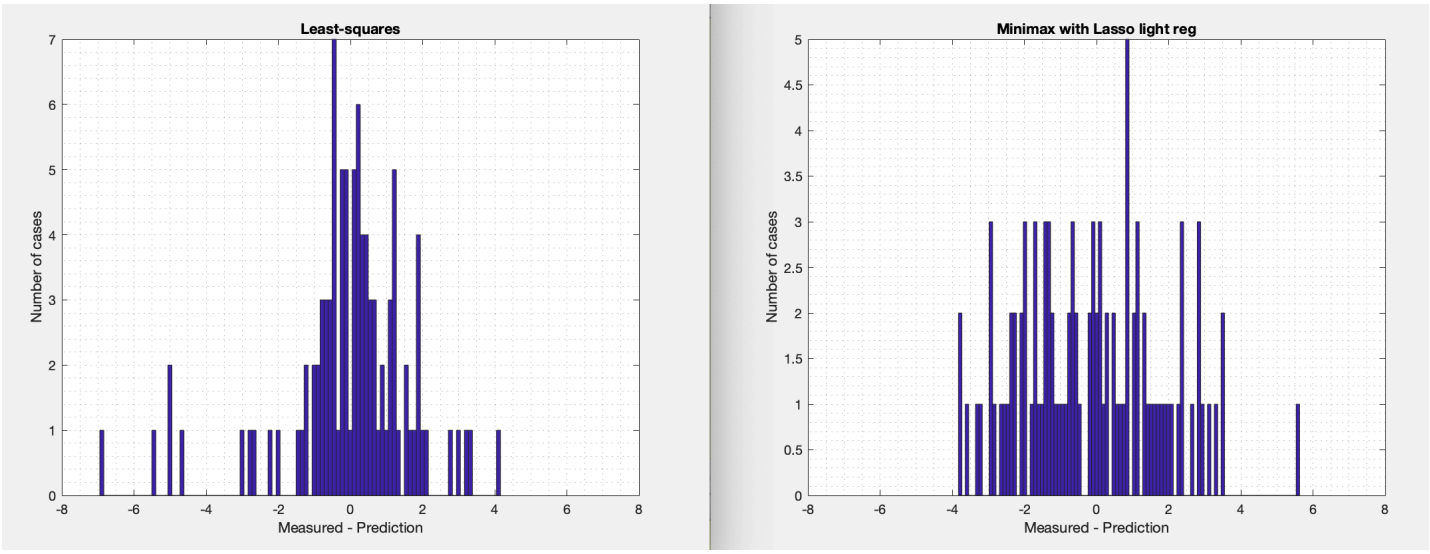

Figure 3. LSE max error for prediction overestimating measurement is 7%, meaning we need to QA all plans having 97% passing rate or lower (79 out of 497, 16.0%) to ensure plans will have 90% or more passing criteria. Minimax prediction error is 4%, meaning we need to QA all plans 94% or lower (24 out of 497, 4.8%) which is 1/4th of the amount that you would need to do with LSE model.

Conclusion and future work: Chebyshev's minimax optimization results in a reduction of the maximum error possible of machine learning algorithms, being the natural selection for Quality Assurance metrics. When applied to IMRT QA data, we showed how it results in a lower maximum error at the expense of a higher average error. This algorithm can selectively choose plans that are more likely to fail QA for the physicist to prioritize resources according to TG 100. Efficient QA programs that ensure safe IMRT treatments require accurate identification of plans that are likely to fail QA criteria. Using Chebyshev minimax optimization, a 95% reduction of resources for IMRT QA can be achieved while meeting current passing criteria.